Finite-size scaling in the interfacial stiffness of rough elastic contacts

Lars Pastewka,[1,2] Nikolay Prodanov,[3,4] Boris Lorenz,[5] Martin H. Müser,[3,4] Mark O. Robbins,[1] and Bo N. J. Persson[5]

[1]*Department of Physics and Astronomy, Johns Hopkins University, Baltimore, Maryland 21218, USA*

[2]*MikroTribologie Centrum μTC, Fraunhofer-Institut für Werkstoffmechanik IWM, 79108 Freiburg, Germany*

[3]*Jülich Supercomputing Center, Institute for Advanced Simulation, FZ Jülich, 52425 Jülich, Germany*

[4]*Department of Materials Science and Engineering, Universität des Saarlandes, 66123 Saarbrücken, Germany*

[5]*Peter Grünberg Institut-1, FZ-Jülich, 52425 Jülich, Germany*

The total elastic stiffness of two contacting bodies with a microscopically rough interface has an interfacial contribution K that is entirely attributable to surface roughness. A quantitative understanding of K is important because it can dominate the total mechanical response and because it is proportional to the interfacial contributions to electrical and thermal conductivity in continuum theory. Numerical simulations of the dependence of K on the applied squeezing pressure p are presented for nominally flat elastic solids with a range of surface roughnesses. Over a wide range of p, K rises linearly with p. Sublinear power-law scaling is observed at small p, but the simulations reveal that this is a finite-size effect. We derive accurate, analytical expressions for the exponents and prefactors of this low-pressure scaling of K by extending the contact mechanics theory of Persson to systems of finite size. In agreement with our simulations, these expressions show that the onset of the low-pressure scaling regime moves to lower pressure as the system size increases.

I. INTRODUCTION

Two solids in mechanical contact tend to touch at only a miniscule fraction of their apparent contact area A_0, because their surfaces are microscopically rough [1–4]. This imperfect contact has profound implications for transmission of charge, heat, and forces through the interface. The effect of the interface can be expressed in terms of an interfacial stiffness or conductance that adds in series with the bulk response of two solids with ideal flat surfaces [5,6]. Improved theories of these interfacial contributions are important because they frequently dominate the total response of the system and are a strong function of the normal force F (or load) pushing the solids together. In this paper, we consider the scaling of stiffness with F for nonadhesive self-affine rough surfaces. The results are more generally applicable since the shear and normal stiffness and electrical and heat conductance are all proportional to each other within linear-response continuum mechanics [6].

In a pioneering experimental work, Berthoud and Baumberger found that the interfacial stiffness was proportional to F for nonadhesive solids with very different elastic properties [5]. The proportionality can be expressed as

$$K = p/u_0, \qquad (1)$$

where K is the interfacial stiffness normalized by A_0, and $p \equiv F/A_0$. The characteristic length u_0 was found to be of the order of the combined root-mean-squared (rms) roughness h_{rms} ($\sim 1\,\mu$m) of the surfaces. The surfaces had self-affine fractal roughness that is common in experiments. Berthoud and Baumberger rationalized their observations within the contact mechanics theory of Greenwood and Williamson [7], which, however, is based on hypotheses that later turned out to be unjustified [8–10]. Nonetheless, the results of additional experiments [11,12] and computer simulations of elastic contacts [11,13–19] with self-affine, fractal roughness are consistent with Eq. (1). Moreover, the proportionality

coefficient u_0 agrees, to within $O(10\%)$, with $u_0 \approx 0.4\,h_{rms}$, derived from the parameter-free contact mechanics theory of Persson [16–18].

The interfacial stiffness can be determined from the total stiffness K_{tot} and the stiffnesses of ideal flat bounding solids K_1 and K_2 using the rule for springs in series

$$K^{-1} \equiv K_{tot}^{-1} - K_1^{-1} - K_2^{-1}. \qquad (2)$$

An alternative approach is to measure—or to compute—the mean interfacial separation $\bar{u}$. Changes in $\bar{u}$ are a direct measure of the deformation attributable to the interface and $K = -dp/d\bar{u}$, where the sign reflects the fact that $\bar{u}$ decreases with increasing confining force. In the range of validity of Eq. (1), this differential relation can be solved to yield another testable prediction,

$$p = p_0 \exp(-\bar{u}/u_0), \qquad (3)$$

where p_0 is an integration constant. Persson theory finds that $p_0 = \beta E^*$, where E^* is the effective elastic modulus and β is dimensionless. Like u_0, β only depends on the spectral properties of the surface [8]. Analytical expressions for u_0 and β and computer simulations agree again to within $O(10\%)$ [15–19].

In a recent letter, Pohrt and Popov [20] challenged the established results on interfacial stiffness by proposing a sublinear $K \propto p^\alpha$ power law deduced from numerical simulations of an indenter with a square punch geometry. Specifically, they reported $\alpha = 0.2567(3 - H)$, where H is the Hurst roughness exponent. This estimate was later corrected to $\alpha = 0.266(3 - H)$ and scaling arguments were presented for a third relation $\alpha = 1/(1 + H)$ [21]. Pohrt *et al.* argued that their results differed from previous ones because their surfaces were "*truly fractal*" [21]; i.e., roughness lived on wavelengths all the way to the linear size L_p of their punch. In particular, they state, "Whenever the surfaces are truly fractal with no cut-off wavelength, a power law applies" [21].

In this paper, we unravel the origin of the discrepancy between the established results and the new findings. To do so, we analyze finite-size effects in numerical simulations. We derive analytical expressions, free of adjustable parameters, that capture finite-size effects and constitute a complete theory for the stiffness of rough contacts. For brevity, we present only the essence of the calculations in the main part of this work. Details on the numerical procedure can be found in Appendix A. The full derivation of prefactors for our scaling theory can be found in Appendix B. Appendix C contains unpublished experiments in support of Persson's contact mechanics theory.

II. NUMERICAL RESULTS

We first summarize the arguments for how Eq. (1) arises from the self-affinity of interfaces [8]. The key idea is that when there are a large number of separated contacting patches, the distribution of contacts is self-similar. As the load increases, existing contact patches grow and new, small contacts are formed. This happens in such a way that the distributions of contact sizes and local pressures remain approximately constant over a wide range of loads [4,22]. An immediate consequence is a linear relation between real contact area A and p, which has been confirmed in many simulations, including all numerical studies cited here. The spatial correlations between contacting areas and local stresses are also the same up to a prefactor that grows linearly with load because of a sum rule [23]. Since the system responds linearly, the elastic energy U_{el} is given by an integral of an elastic Green's function times the Fourier transform of the stress-stress correlation function and must thus be proportional to load:

$$U_{el} = u_0 A_0 p. \qquad (4)$$

Since the elastic energy is equal to the work done by the external load (assuming hard-wall interactions and no adhesion), it follows that $dU_{el} = u_0 A_0 dp \equiv -A_0 p(\bar{u}) d\bar{u}$. This last relation is identical to Eq. (3) and thus also to Eq. (1).

When p is so small that two *finite* surfaces start touching, the interface cannot yet behave in a self-similar fashion. The reason is that contact occurs only near the highest asperity whose height determines the separation at first contact u_c. As a consequence, the validity of the arguments leading to Eq. (4) and thus to Eq. (1)—or any theory valid in the thermodynamic limit—cannot hold at small p. As already pointed out earlier, finite-size effects then become important [12]. Specifically, for a finite system p vanishes for (finite) $\bar{u} > u_c$, while for an infinite system p is always nonvanishing. Thus, p must initially decay faster with increasing $\bar{u}$ in a finite system than in an infinite system where Eq. (1) holds. In the opposite case of large p, a finite system approaches complete contact, $\bar{u} = 0$, at finite pressure but infinite systems do not because they have infinitely deep valleys. One may conclude that contact formation of the highest peak and the lowest valley depend on the specific realization of a surface. However, for intermediate pressures, universal behavior may be found as long as the roughness has well-defined statistical properties.

To study finite-size effects, we performed large-scale numerical simulations of nonadhesive contact between a rigid self-affine surface and an isotropic elastic substrate with effective modulus E^* and Poisson number 0.5 using well-
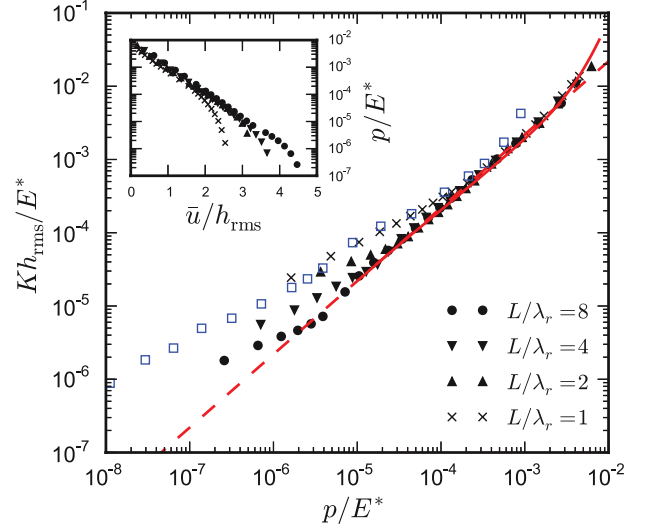

FIG. 1. (Color online) Log-log plot of the nondimensional contact stiffness $K h_{rms}/E^*$ vs. nondimensional pressure p/E^* for self-affine fractal surfaces with $H = 0.7$ and rms slope $h'_{rms} = 0.1$. In all cases, the surface is resolved with 8192 points in each direction, $L/\lambda_1 = 4096$, and the ratio of system size to roll-off wavelength, L/λ_r, is indicated. The (red) solid line is the prediction of Persson's theory while the dashed (red) line is the linear regime. Open squares (blue) show the interfacial stiffness obtained from a punch calculation with $L_p/\lambda_1 = 1024$. Inset: Nondimensional pressure vs. separation for the same surfaces.

established methods [24,25] that are discussed in more detail in Appendix A. Periodic boundary conditions were applied to a square region of length L. Surfaces were self-affine with Hurst exponent H between a short wavelength cut-off λ_1 and long-wavelength roll-off λ_r (see Fig. 4). The amplitudes of the Fourier transforms for the height $\tilde{h}(\mathbf{q})$ were drawn from a Gaussian distribution. Their variances reflect the roughness spectrum $C(q)$ for each reciprocal space vector $\mathbf{q}$:

$$C(q) = C_0 \begin{cases} 1 & \text{for } q_0 < q < q_r \\ (q/q_r)^{-2-2H} & \text{for } q_r \leqslant q \leqslant q_1 \\ 0 & \text{for } q_1 < q. \end{cases} \qquad (5)$$

Here, $q_0 = 2\pi/L$, $q_1 = 2\pi/\lambda_1$, and $q_r = 2\pi/\lambda_r$ and the desired self-affine scaling is reflected in the power law for the range $q_r \leqslant q \leqslant q_1$.

Figure 1 shows typical results for the contact stiffness versus pressure. Note that all the quantities are made dimensionless by dividing by the modulus and rms roughness so that they can be mapped to any experimental system with the same surface statistics. In all cases, there is a linear relation at intermediate loads and a more rapid rise of K with p as full contact is approached. Both regimes are well-described by Persson's contact mechanics theory (red line), which requires only the surface roughness power spectrum and the effective modulus as input. We also find a transition to power-law scaling at low loads. This transition is particularly sensitive to the magnitude of a few random Fourier components at the smallest wavevectors as well as to their relative phases. The separation at first contact u_c is also very sensitive to these Fourier components and decreases with L/λ_r. It cuts off the exponential relation between p and u shown in the inset.

Even for the case where $L/\lambda_r = 1$, the results in Fig. 1 follow linear scaling [Eq. (1)] for more than one decade. The range of validity of the linear scaling regime extends rapidly to lower p as L/λ_r increases. Thus, the more closely the thermodynamic limit is approached—or the more significant the statistical distribution of contacting peaks—the more accurate is Eq. (1). Given typical λ_r, e.g., $O(10\,\mu\text{m})$ for polished steel and $O(1\,\text{cm})$ for asphalt, one can see that power-law scaling matters only if $L/\lambda_r \approx 1$ or when loads are small. Additionally, at extremely small loads, where the first asperities are touching, the behavior should be Hertzian with $K \propto p^{1/3}$ if $\lambda_1 > 2a_0$ where a_0 is the grid size of the numerical method (see Appendix A). Indeed, we find that reducing the ratio of λ_r/λ_1 gives an exponent that approaches the one expected from Hertz contact mechanics. Earlier reports of Hertzian-like behavior in load versus area for $\lambda_1 > a_0$ [26] are consistent with this finding. This additional scaling regime limits the range where power-law scaling should be observed and complicates its measurement in simulations.

The results of Ref. [20] do not show any appreciable region of linear scaling. We have repeated their calculations to determine the origin of this discrepancy. Instead of the periodic boundary conditions used here, they considered a rigid, square punch with edge L_p contacting an infinite elastic substrate. The punch had fractal roughness on all wavelengths from $\lambda_1 = 2a_0$ to L_p. The open squares (blue) in Fig. 1 show results for this geometry (see also Appendix A). The interfacial stiffness was extracted from Eq. (2) and the analytical punch solution [27]. While this correction is not performed in Ref. [20], it has little effect at the low loads of greatest interest.

At low loads, results for the flat punch and periodic boundary conditions follow the same power-law scaling. However, as in Ref. [20], the flat punch results cross over to a rapid rise with no region of linear scaling. Inspection of the results shows that this behavior is associated with strong artifacts from the boundary conditions at the edge of the punch. The analytic solution for the pressure under a flat punch has a singularity at the punch edges. The solution for a rough punch approaches this solution as the pressure increases. The pressure and stiffness are all dominated by regions near the edge, which approach full contact long before the central regions. The strong influence of the edge makes the problem effectively one dimensional, which may explain the success of the dimensional reduction used in Ref. [21] to fit their results.

III. SCALING THEORY

In the low load regime, Fig. 1 indicates $K \propto p^\alpha$ behavior with $\alpha \approx 0.6$ for $H = 0.7$. Thus, our small-pressure results for $L/\lambda_r = 1$ are consistent with Refs. [20,21]. In the following, we propose a new explanation for this power law by incorporating the estimation of finite-size effects into Persson's contact mechanics theory. The goal is to find an expression for the elastic energy because it allows us to calculate the contact stiffness. We reexpress a small change of the elastic energy $dU_{\text{el}} = -pA_0 d\bar{u}$ as $dU_{\text{el}} = -pA_0 dp(d\bar{u}/dp)$. Inserting $K = -dp/d\bar{u}$ and $F = pA_0$ yields

$$p = K\frac{dU_{\text{el}}}{dF}. \qquad (6)$$

Our approach is motivated by the fact that the elastic energy is dominated by the longest wavelength modes [16]. For a single contacting region around the highest peak, the longest wavelength will scale with the radius r_0 of the smallest circle that encloses the contacts. We will first calculate the elastic energy $U_{\text{el}}^{(0)}$ for a single Hertzian-like mesoscale asperity with radius of curvature R and contact radius r_0. Then we show that including roughness on the mesoasperity at wavelengths smaller than r_0 gives the same power-law scaling for the elastic energy $U_{\text{el}}^{(1)}$. For brevity, what follows presents only the general scaling arguments that explain the observed power law. A general derivation, including all prefactors, is given in Appendix B.

An effective asperity radius is calculated from the roughness at scales larger than r_0. The local curvature $\nabla^2 h$ corresponds to $q^2 h(q)$ in Fourier space. Thus, R can be estimated as:

$$\frac{1}{R^2} \propto \int_{q_0}^{\pi/r_0} d^2q \, |q^2 h(q)|^2 \propto \int_{q_0}^{\pi/r_0} dq \, q^5 C(q). \qquad (7)$$

For self-affine fractal roughness, the surface roughness power spectrum is $C(q) \propto q^{-2-2H}$. This gives $R \propto r_0^{-H}$, where we have assumed that the lower integration bound to the last integral must be negligible at a small load. This condition is fulfilled as long as $r_0 \ll \lambda_r$.

According to Hertzian contact mechanics, $r_0 \propto (RF)^{1/3}$. Inserting $R \propto r_0^{2-H}$ and solving for r_0, we obtain

$$r_0 \propto F^{1/(1+H)}. \qquad (8)$$

The elastic energy stored within a Hertzian contact is $U_{\text{el}}^{(0)} \propto F\delta$, where the penetration depth $\delta \propto r_0^2/R \propto r_0^H$. We obtain

$$U_{\text{el}}^{(0)} \propto F^{(1+2H)/(1+H)} \qquad (9)$$

and from Eq. (6)

$$K \propto p^{1/(1+H)}. \qquad (10)$$

We now show that the elastic energy $U_{\text{el}}^{(1)}$ due to microscale roughness within the mesoscale asperity also scales with $F^{(1+2H)/(1+H)}$. The main assumption now is that the contact pressure within the mesoscale asperity contact region is high enough that the contact mechanics theory by Persson can be applied. Then, from Eq. (4), $U_{\text{el}}^{(1)} = u_1 A_1 p_1$, where $A_1 = \pi r_0^2$ is the (nominal) contact area at the mesoscale and $p_1 = F/A_1$. The term u_1 is of the order of the rms roughness, including only roughness components with wavelength $\lambda < r_0$. This can be written as

$$\left(h_{\text{rms}}^{\text{meso}}\right)^2 = 2\pi \int_{\pi/r_0}^{2\pi/\lambda_1} dq \, q C(q) \propto \left(\frac{\pi}{r_0}\right)^{-2H} - \left(\frac{2\pi}{\lambda_1}\right)^{-2H}. \qquad (11)$$

Since $\lambda_1 \ll r_0$ (unless H is close to 0), one obtains $h_{\text{rms}}^{\text{meso}} \propto r_0^H$ and $u_1 \propto r_0^H$. Inserting $r_0 \propto F^{1/(1+H)}$, we get $U_{\text{el}}^{(1)} \propto F^{(1+2H)/(1+H)}$ as in Eq. (9).

From the above treatment we predict that the stiffness K scales as p^α with $\alpha = 1/(1+H)$. Figure 2 shows $K(p)$ relations obtained numerically in the finite-size regime for different values of H. Rough estimates for α were obtained by fitting to the lowest four data points. The results from
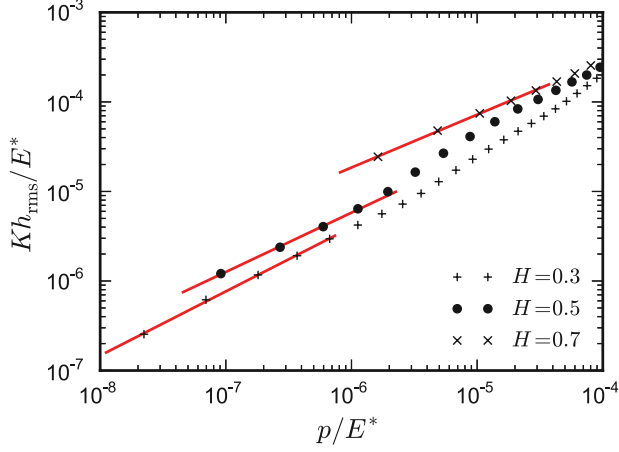
FIG. 2. (Color online) Dimensionless interfacial stiffness Kh_{rms}/E^* as a function of pressure p/E^* in the finite-size region for $L/\lambda_1 = 4096$ and different Hurst exponents H. All calculations are for $L/\lambda_r = 1$. Solid lines show a fit to the first four data points.
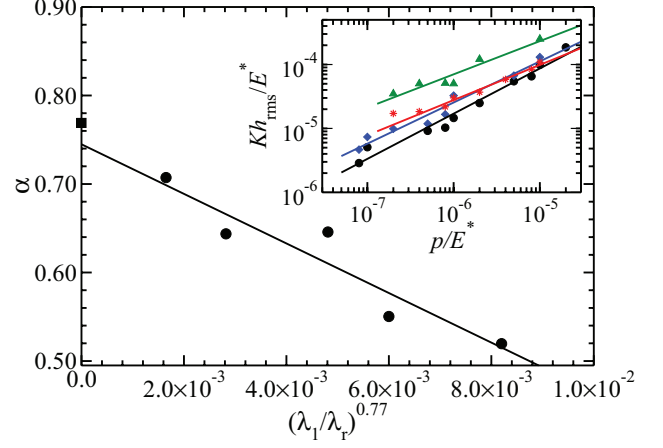

FIG. 3. (Color online) Exponent α as a function of $(\lambda_1/\lambda_r)^{0.77}$. Theoretically predicted value is denoted by ■. The inset shows selected numerical data for $K(p)$ from which α was deduced. Data for the following values of λ_r/λ_1 is presented: 4096 (●), 2048 (♦), 768 (∗), 512 (▲).

the simulations are: $\alpha(H = 0.3) = 0.72$ (see also below), $\alpha(H = 0.5) = 0.66$, and $\alpha(H = 0.7) = 0.59$. These values compare well to the theoretical predictions, $\alpha(H = 0.3) \approx 0.769$, $\alpha(H = 0.5) \approx 0.667$, and $\alpha(H = 0.7) \approx 0.588$, particularly if one keeps in mind that systematic simulation errors increase as H approaches zero.

We note here that the expression for the microasperity contribution to the total elastic energy depends on the elastic coupling between the asperities. Any derivation neglecting this coupling [20] cannot describe the correct physics, even if the resulting scaling is similar to $K \propto p^{1/(1+H)}$. Moreover, probing the constitutive relation between pressure and stiffness at a mesoscale will entail much larger fluctuations than in a multiasperity contact at the same pressure but larger value of L/λ_r.

The arguments that lead to $K \propto p^{1/(1+H)}$ hold when $\lambda_1 \ll r_0 \ll \lambda_r$. Since $R \propto r_0^{2-H}$, the radius of the mesoasperity diverges as the contact area grows and $r_0 \to \lambda_r$. In this limit, the mesoasperities are flat, both Eqs. (2) and (3) hold, and we rediscover the thermodynamic limit $K \propto p$ [15–19]. On the other hand, if $r_0 < \lambda_1$, the surface of the mesoasperity is smooth. The upper integration bound in Eq. (7) is then given by the short wavelength cut-off $q_1 = 2\pi/\lambda_1$, and R is constant. This ultimately must lead to traditional Hertz behavior where $K \propto p^{1/3}$. Figure 3 shows the results of an attempted extrapolation to the "fractal limit" $\lambda_1/\lambda_r \to 0$ for the value of $H = 0.3$, which had the largest discrepancy between theory and simulation. Despite quite large stochastic scatter, we conclude that the value of $\alpha = 1/(1 + H)$ is consistent with the simulations.

Finally, we address how the finite-size power-law region depends on linear system size L and roll-off length λ_r. Following along the lines of the above derivation, it is straightforward to compute the full expression for the interfacial stiffness (see Appendix B):

$$\frac{Kh_{\mathrm{rms}}}{E^*} = \theta \left(\frac{h_{\mathrm{rms}}}{2\pi \lambda_r} \frac{\lambda_r^2}{L^2} \right)^{H/(1+H)} \left(\frac{p}{s^{1/2} E^*} \right)^{1/(1+H)}, \qquad (12)$$

where $1/s = 1 + H[1 - (\lambda_r/L)^2]$. The prefactor θ depends only on the Hurst exponent H, but for $H > 0.3$ variation is restricted to $0.75 \lesssim \theta \lesssim 1.0$ (see also Fig. 5). By equating Eq. (12) with $K = p/\gamma h_{\mathrm{rms}}$, where $\gamma \approx 0.4$, we obtain an estimate for the pressure p_c at which the stiffness crosses over from power law to linear behavior:

$$\frac{p_c}{E^*} = \frac{h_{\mathrm{rms}}}{2\pi \lambda_r} \frac{\lambda_r^2}{L^2} s^{-1/2H} (\theta \gamma)^{(1+H)/H} . \qquad (13)$$

For different realizations of the surface, the prefactor of the power law and p_c can vary significantly. Nevertheless, for the data shown in Fig. 1 we find $p_c/E^* \approx 6 \times 10^{-5}$ for $q_r/q_0 = 1$ and $p_c/E^* \approx 3 \times 10^{-6}$ for $q_r/q_0 = 8$, in excellent agreement with the numerical data. Generally, the cross-over pressure p_c decreases with increasing linear system size L. Equation (13) also reveals the importance of separation between L and the roll-off length λ_r. Scale separation pushes the crossover to lower pressure even more rapidly since the ratio L/λ_r enters quadratically. In the thermodynamic limit $L/\lambda_r \to \infty$, the power-law region vanishes all together.

IV. CONCLUSIONS

We conclude that the previously reported $K \propto p$ and $p \propto \exp(-\bar{u}/u_0)$ laws [11–19] are satisfied when there is a statistical ensemble of high peaks in contact. This linear scaling extends to lower loads as the upper length scale of roughness decreases, because there is a better statistical sampling of high peaks. At the smallest loads, the contact diameter is smaller than the smallest wavelength of roughness, and the stiffness follows the Hertz expression for contact of a single spherical asperity, $K \propto p^{1/3}$. At slightly larger contact areas and loads, contact is confined to a single large peak with a fractal hierarchy of smaller bumps. In this regime, K scales sublinearly with p and the prefactor and corresponding surface separation have large fluctuations from one sample to the next, even in the limit of large system size. Parameter-free expressions for the power law $\alpha = 1/(1 + H)$ and prefactor

[Eq. (12)] were derived. The power law agrees with one of the results presented in Ref. [21], although they also presented linear $\alpha \propto H$ expressions [20,21] when fitting their numerical data. Reference [21] also discussed the scaling of the prefactor with L but we provide a full expression including the dependence on rolloff λ_r and Hurst exponent H.

Pohrt, Popov, and Filippov (Refs. [20,21]) found no linear regime in their studies of stiffness. In part this was because they considered the limiting case of roughness at wavelengths up to the size of their contact ($\lambda_r = L_p$). As recently pointed out by Barber [28], statistical fluctuations make a prediction of stiffness (and related properties such as conductance) difficult if there is no separation between the scales of the macroscopic object and the longest wavelength of the roughness. For nominally flat surfaces and periodic boundary conditions, we observe that the linear $K \propto p$ regime holds for at least an order of magnitude in load even in this extreme case. The square punch geometry considered in Ref. [20] suppresses this linear regime (Fig. 1). Stress is concentrated near the edges of the punch, which approach full contact long before the central region. This pronounced heterogeneity makes the punch geometry a poor choice and it is rarely used in experiments because of the difficulty in achieving perfect alignment [29].

Most experimental realizations of surfaces have an rms roughness and upper cut-off on fractal scaling that are both significantly smaller than the system size. As a result, Eq. (13) predicts that the linear relation between stiffness and load should extend over the experimental range. Indeed, measurements by Berthoud and Baumberger [5] show $K \propto p$ even at fractional contact areas of 10^{-6} and below. We conclude that as long as the contact responds elastically, the power-law region appears to be confined to low pressure that is difficult to access in macroscopic experiments and has, therefore, little impact on most applications.

As an example, consider applications to syringes, where the relation between the squeezing pressure p and the average interfacial separation $\bar{u}$ (which determines the contact stiffness) is very important for the fluid leakage at the rubber-stopper barrel interface [30]. The key contact region is between a rib of the rubber stopper and the barrel. The width of the contact region (of order $w \approx 1$ mm) defines the cut-off wavevector $q_r = 2\pi/w \approx 6000$ m^{-1}. The Hurst exponent $H \approx 0.9$ and the rms roughness amplitude (including the roughness components with wavevector $q > q_r$) is $h_{\text{rms}} \approx 3$ μm. The elastic modulus of the rubber stopper is typically $E \approx 3$ MPa. Using these parameters, we find from Eq. (13) that the stiffness should rise linearly with pressure above $p_c \approx 1$ kPa. This is negligible compared to the pressure in the contact region between the rib of the rubber stopper and the barrel, which is typically of order 1 MPa.

As devices shrink toward the nanoscale, h_{rms} and λ_r may become closer to the system size. For example, Buzio *et al.* [31] report nonlinear stiffness when loading flat contacts of size $L_p \sim 2$ μm on rough surfaces with $h_{\text{rms}} \sim 20$ to 100 nm and $\lambda_L \sim 1$ μm up to forces of 200 nN. Equation (13) predicts nonlinear behavior for these parameters, but the experimental tips were adhesive, there was evidence of plastic deformation, and atomistic effects may become important at nanometer scales [32]. None of these effects has been included here or

in Refs. [20,21], and future work on their influence will be of great interest

APPENDIX A: DETAILS OF THE NUMERICAL CALCULATIONS

Self-affine rough surfaces with the desired H, h'_{rms}, λ_s, and λ_L were generated using a Fourier-filtering algorithm described previously [10]. Fourier components for each wavevector $\mathbf{q}$ have a random phase and a normally distributed amplitude that depends on the wavevector magnitude q according to Eq. (5). Periodic boundary conditions with period L were applied in the plane of the surface to prevent edge effects. Figure 4 shows a roughness power spectrum as generated by this algorithm and used in the simulations. The solid lines indicate the mean values for the spectrum, while the dots reflect one particular realization. Fluctuations of the height $h(\mathbf{r})$ in real space are not only the consequence of variations in the absolute value of their complex Fourier transforms $\tilde{h}(\mathbf{q})$ but also due to the random phases. From Fig. 4 it becomes clear that the largest fluctuations occur at small wavevectors (large wavelength) because $O(q^2)$ Fourier components contribute to the power spectrum for wavevectors of magnitude q.

We considered elastic substrates with contact modulus E^* and Poisson ratio $\nu = 1/2$. At $\nu = 1/2$, the in-plane components and the out-of-plane components of the elastic displacement field decouple. We then only treated the out-of-plane components $u(\mathbf{r})$ on a grid with spacing a_0. More specifically, we carried out simulations with $E^* = 2$ and $a_0 = 1$, but since all quantities are presented here in a dimensionless form, the actual values of these quantities do not matter. The elastic interaction was solved using a Fourier-transform technique [24,25] that accelerates computation of the force $f(\mathbf{r}) = \int d^2 r' G^{-1}(\mathbf{r} - \mathbf{r}') u(\mathbf{r}')$. For periodic calculations, we used a linearized surface Green's function [25,33]. In reciprocal space, the expression for the Green's function is $\tilde{G}^{-1}(\mathbf{q}) = E^* q/2$. For nonperiodic calculations, we employed a real-space surface Green's function $G(\mathbf{r})$ that is derived from the elastic response to a uniform pressure on a square region of area a_0^2 [34]. A padding region was used to separate repeating images [35].

APPENDIX B: FULL SCALING THEORY, INCLUDING DERIVATION OF ALL PREFACTORS

Consider a randomly rough surface with a power spectrum given by Eq. (5) and shown in Fig. 4. The surface mean-square
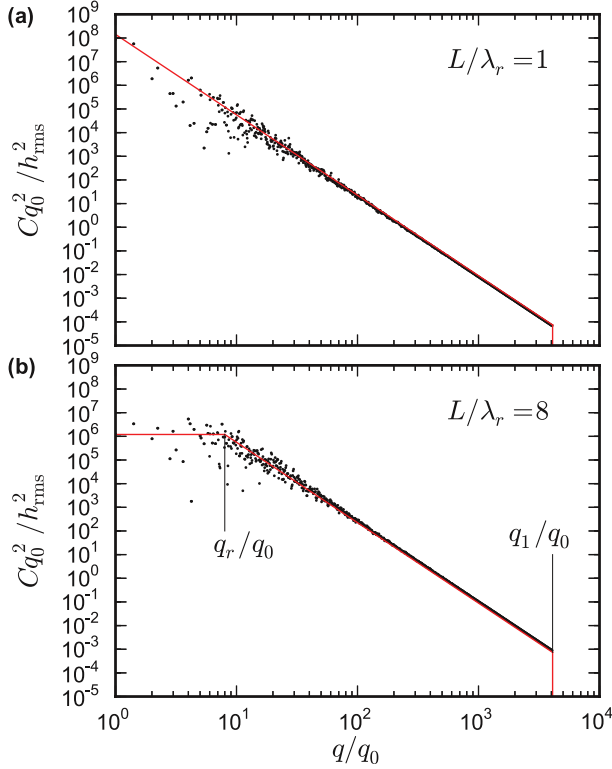
(a)

(b)

FIG. 4. (Color online) Power spectra for two surfaces without (a) and with (b) a roll-off at large wavelength as generated by a Fourier filtering algorithm. The solid lines show the prescribed power spectrum $C(q)$ and the dots the actual realization. Panel (b) indicates the wavevectors of the long-wavelength roll-off $q_r = 2\pi/\lambda_r$ and the short-wavelength cut-off $q_1 = 2\pi/\lambda_1$. For $q < q_0 = 2\pi/L$, where L is the linear system size, the surfaces have zero power. The noise at low q is due to the fact that order q^2 Fourier components contribute to the power spectrum at wavevector q of a realization of a surface.

roughness amplitude is then given by

$$h_{\rm rms}^2 = \int d^2q \, C(q) \tag{B1}$$

$$= 2\pi C_0 \left[\int_{q_0}^{q_r} dq \, q + \int_{q_r}^{q_1} dq \, q \left(\frac{q}{q_r} \right)^{-2-2H} \right] \tag{B2}$$

$$\approx \frac{\pi q_r^2}{Hs} C_0, \tag{B3}$$

where $1/s = 1 + H[1 - (q_0/q_r)^2]$ and the last equality holds in the limit $q_1/q_r \gg 1$. Note that $s = 1$ if $q_0 = q_r$ and there is no roll-off region. Expressed in terms of $h_{\rm rms}$, the normalization of the power spectrum is

$$C_0 = \frac{Hs}{\pi q_r^2} h_{\rm rms}^2. \tag{B4}$$

1. Hertzian-like mesoscale asperity

We first calculate the elastic energy stored in the deformation field associated with the Hertz mesoscale asperity contact region. The mesoscale asperity has the radius of curvature R. The radius of the (apparent) contact region between the mesoscale asperity and the flat countersurface is denoted by r_0. We assume that no roughness lives on scales $<r_0$, such that

the mesoscale asperity can be treated as smooth. The mean summit asperity curvature is given by [36] $\bar{\kappa} = \beta \sqrt{2\kappa_0}$, where κ_0 is the root-mean-square curvature of the surface:

$$\kappa_0^2 = \frac{1}{2} \int d^2q \, q^4 C(q) = \pi \int_{q_0}^{q_1} dq \, q^5 C(q). \tag{B5}$$

Nayak [36] has shown that $\beta = \sqrt{8/3\pi}$ when roughness occurs on many length scales so that $q_1/q_0 \gg 1$. If we include only roughness components with wavevector $q < \pi/r_0$, then we obtain the mean summit curvature $1/R$ of the mesoscale asperity:

$$\frac{1}{R^2} = 2\pi\beta^2 \int_{q_0}^{\pi/r_0} dq \, q^5 C(q). \tag{B6}$$

We now define the dimensionless quantities $\bar{R} = q_r R$, $\bar{h}_{\rm rms} = q_r h_{\rm rms}$, and $\bar{r}_0 = q_r r_0$. This gives the mean dimensionless summit curvature

$$\frac{1}{\bar{R}^2} = \frac{2\pi\beta^2 C_0}{q_r^2} \left[\int_{q_0}^{q_r} dq \, q^5 + \int_{q_r}^{\pi/r_0} dq \, q^5 \left(\frac{q}{q_r} \right)^{-2-2H} \right] \tag{B7}$$

$$\approx \frac{Hs\beta^2}{2-H} \bar{h}_{\rm rms}^2 \left(\frac{\pi}{\bar{r}_0} \right)^{4-2H}, \tag{B8}$$

where the last equality holds in the limit $\pi/r_0 \gg q_r$. We define the dimensionless prefactor

$$\chi = \left(\frac{2-H}{Hs} \right)^{1/2} \frac{\pi^{H-2}}{\beta \bar{h}_{\rm rms}}. \tag{B9}$$

and simplify Eq. (B8) to

$$\bar{R} = \chi \bar{r}_0^{2-H}. \tag{B10}$$

We now use Hertz theory to obtain the mesoasperity radius r_0 as a function of normal force F. Hertz theory gives a dimensionless mesoasperity contact radius of

$$\bar{r}_0^3 = \frac{3}{4} \bar{F}\bar{R} = \frac{3\chi}{4} \bar{F}\bar{r}_0^{2-H}, \tag{B11}$$

where $\bar{F} = F q_r^2 / E^*$ is the dimensionless normal force and we used Eq. (B10) for the dimensionless asperity radius. We now solve for $\bar{r}_0$ to obtain

$$\bar{r}_0 = \left(\frac{3\chi}{4} \bar{F} \right)^{1/(1+H)}. \tag{B12}$$

By inserting this expression into Eq. (B10), the mesoasperity radius becomes

$$\bar{R} = \chi^{3/(1+H)} \left(\frac{3}{4} \bar{F} \right)^{(2-H)/(1+H)}. \tag{B13}$$

The elastic energy stored in the Hertz mesoscale deformation field for depth of indentation δ is given by

$$\bar{U}_{\rm el}^{(0)} = \frac{2}{5} \bar{F}\bar{\delta}, \tag{B14}$$

where $\bar{\delta} = q_r \delta$ and the dimensionless energy $\bar{U}_{\rm el}^{(0)} = U_{\rm el}^{(0)} q_r^3 / E^*$. Hertz theory also tells us the displacements as a function of normal force,

$$\bar{\delta} = \left(\frac{9\bar{F}^2}{16\bar{R}} \right)^{1/3} = \chi^{-1/(1+H)} \left(\frac{3}{4} \bar{F} \right)^{H/(1+H)}, \tag{B15}$$

where we used Eq. (B13) to substitute the mesoasperity radius. By combining Eqs. (B14) and (B15), the elastic energy becomes

$$\bar{U}_{el}^{(0)} = \frac{4}{3}\kappa_0 \chi^{-1/(1+H)} \left(\frac{3}{4}\bar{F}\right)^{(1+2H)/(1+H)}, \qquad (B16)$$

with $\kappa_0 = 2/5$.

2. Microscale roughness on mesoscale asperity

Next we calculate the elastic deformation energy that is stored in microasperity contacts within the Hertz mesoasperity contact region [8,16]. This energy is given by Eq. (4):

$$U_{el}^{(1)} = u_1 A p_1 = u_1 F. \qquad (B17)$$

In terms of the dimensionless quantities, it becomes $\bar{U}_{el}^{(1)} = \bar{u}_1 \bar{F}$, where $\bar{u}_1 = q_r u_1$. Additionally, we have $\bar{u}_1 = \gamma(\bar{h}_{rms}^{meso})$, where $\gamma \approx 0.4$. Note that h_{rms}^{meso} is the root-mean-square roughness amplitude within the mesoasperity, i.e., within the area confined by the mesoasperity contact radius r_0. In contrast, h_{rms} is the root-mean-square roughness amplitude of the full surface all the way to the linear system size L. We can express h_{rms}^{meso} in terms of h_{rms}:

$$\left(h_{rms}^{meso}\right)^2 = 2\pi C_0 \int_{\pi/r_0}^{q_1} dq\, q \left(\frac{q}{q_r}\right)^{-2-2H} \qquad (B18)$$

$$\approx s h_{rms}^2 \left(\frac{\pi/r_0}{q_r}\right)^{-2H}. \qquad (B19)$$

This holds for $\pi/r_0 \ll q_1$. In terms of the dimensionless quantities, this becomes

$$\bar{h}_{rms}^{meso} = s^{1/2} \bar{h}_{rms} \left(\frac{\pi}{\bar{r}_0}\right)^{-H}. \qquad (B20)$$

We now use the definition for χ [Eq. (B9)] to eliminate $\bar{h}_{rms}$ and use Eq. (B12) to express $\bar{r}_0$ in terms of the force $\bar{F}$:

$$\bar{h}_{rms}^{meso} = \left(\frac{2-H}{\pi^4 \beta^2 H}\right)^{1/2} \chi^{-1/(1+H)} \left(\frac{3}{4}\bar{F}\right)^{H/(1+H)}. \qquad (B21)$$

By combining Eqs. (B17) and (B21), the elastic energy becomes

$$\bar{U}_{el}^{(1)} = \frac{4}{3}\kappa_1 \chi^{-1/(1+H)} \left(\frac{3}{4}\bar{F}\right)^{(1+2H)/(1+H)}, \qquad (B22)$$

with

$$\kappa_1 = \gamma \left(\frac{2-H}{\pi^4 \beta^2 H}\right)^{1/2}. \qquad (B23)$$

Note that the expression for $\bar{U}_{el}^{(1)}$ has the same form as the expression derived for the Hertz-like mesoasperity contact Eq. (B16). They differ only in the prefactors κ_0 and κ_1.

3. Total elastic energy and stiffness

The total elastic energy is now given by the sum of the two contributions Eqs. (B16) and (B22), i.e., $\bar{U}_{el} = \bar{U}_{el}^{(0)} + \bar{U}_{el}^{(1)}$. This yields

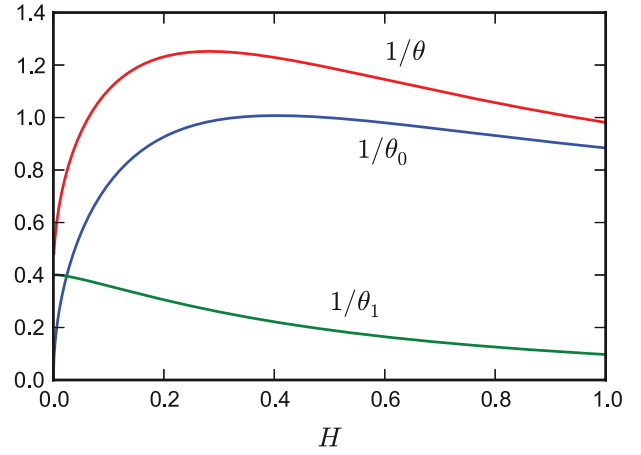$$\bar{U}_{el} = \frac{4}{3}\kappa \chi^{-1/(1+H)} \left(\frac{3}{4}\bar{F}\right)^{(1+2H)/(1+H)}, \qquad (B24)$$

FIG. 5. (Color online) Plot of the values of $1/\theta_0$, $1/\theta_1$, and $1/\theta = 1/\theta_0 + 1/\theta_1$ as a function of Hurst exponent H. The quantities θ_0 and θ_1 are defined in the text.

with $\kappa = \kappa_0 + \kappa_1$. We now compute the total dimensionless stiffness $\bar{k} = q_r K A_0/E^*$ from Eq. (6). It is given by

$$\bar{k} = \frac{\bar{F}}{d\bar{U}_{el}/d\bar{F}}, \qquad (B25)$$

and inserting Eq. (B24) yields

$$\bar{k} = \theta \left(\frac{\bar{F}}{\bar{h}_{rms} s^{1/2}}\right)^{1/(1+H)}. \qquad (B26)$$

Reintroducing the dimensional quantities yields Eq. (12).

The dimensionless prefactor θ is given by the sum of two contributions, $1/\theta = 1/\theta_0 + 1/\theta_1$, which both depend on the Hurst exponent H only:

$$\frac{1}{\theta_{0/1}} = \frac{1+2H}{1+H} \left(\frac{3}{4\pi}\right)^{H/(1+H)} \left(\frac{\pi^4 \beta^2 H}{2-H}\right)^{1/(2+2H)} \kappa_{0/1}. \qquad (B27)$$

In Fig. 5, we show $1/\theta_0$, $1/\theta_1$, and $1/\theta$ as a function of the Hurst exponent H. It is interesting to note that as $H \to 0$, then $1/\theta_0 \to 0$, while $1/\theta_1$ remains finite; i.e., for the fractal dimension $D_f = 3 - H = 3$, the stiffness is entirely determined by the short-wavelength roughness in the mesoasperity contact region. Note also that since $q_r \approx \pi/L$, where L is the linear size of the system, the stiffness scales as $k \sim q_r^{-H/(1+H)} \sim L^{H/(1+H)}$ with the size of the system. This is in contrast to the region where $p \sim \exp(-u/u_0)$. There, the interfacial contact stiffness is independent of the size L of the system. Note also that the stiffness scales with the rms roughness as $h_{rms}^{-1/(1+H)}$, while in the region $p \sim \exp(-u/u_0)$ the stiffness is proportional to h_{rms}^{-1}. For the Hurst exponent $H \approx 0.8$, which is typical in practical applications, $\theta \approx 1$, which appears to be in good agreement with the prefactor found by Pohrt and Popov in their numerical simulation study [20]. The treatment presented above can be generalized to obtain the distribution of stiffness values (at least approximately) by calculating the distribution $P(R)$ of summit curvature radius R.

It is interesting to determine the critical force, F_c, such that for $F < F_c$ one needs to use the finite-size power-law

expression for the stiffness, while for $F > F_c$ the Persson expression is valid. When the relation $p \sim \exp(-\bar{u}/u_0)$ is valid, the stiffness is given by Eq. (1):

$$\bar{k} = \frac{\bar{F}}{\bar{u}_0} = \frac{\bar{F}}{\gamma \bar{h}_{\rm rms}}. \tag{B28}$$

The critical force F_c is determined by the condition that $\bar{k}$ given by Eqs. (B26) and (B28) coincide. This gives

$$\theta \left(\frac{\bar{F}_c}{\bar{h}_{\rm rms} s^{1/2}} \right)^{1/(1+H)} = \frac{\bar{F}_c}{\gamma \bar{h}_{\rm rms}}, \tag{B29}$$

which we can solve for the dimensionless critical force $\bar{F}_c$:

$$\frac{\bar{F}_c}{\bar{h}_{\rm rms}} = s^{-1/2H} (\theta \gamma)^{(1+H)/H}. \tag{B30}$$

Reintroducing dimensional quantities yields Eq. (13).

4. Discussion

The prediction [Eq. (13)] for the switching between the finite-size region and the region where the stiffness is proportional to the loading force is in good agreement with our simulation results. The surfaces we have studied in numerical simulations have rms slope $h'_{\rm rms} = 0.1$ and $q_0/q_1 = 1/4096$ and $H = 0.7$. For our particular realizations, we find $q_r h_{\rm rms} \approx 5.7 \times 10^{-3}$ for $q_r/q_0 = L/\lambda_r = 1$ and $q_r h_{\rm rms} \approx 1.3 \times 10^{-2}$ for $q_r/q_0 = 8$. With these numbers we get $p_c/E^* \approx 6 \times 10^{-5}$ for $q_r/q_0 = 1$ and $p_c/E^* \approx 3 \times 10^{-6}$ for $q_r/q_0 = 8$ from Eq. (13), which is in good agreement with Fig. 1. For the surface with $H = 0.3$, we obtain (for a surface with rms slope 0.1) $q_r h_{\rm rms}$ nearly 100 times smaller than for $H = 0.7$, which will shift the crossover force F_c, between the two stiffness regions, with a similar factor to lower values, again in good agreement with the numerical studies. The results presented above differ from the conclusion of Pohrt and Popov, who state that the power-law relation observed for small applied forces is valid for all applied forces [20,21]. The present study shows that this statement is incorrect, and Fig. 1 clearly shows that the contact stiffness cannot be described by a power law for all applied forces, as this would correspond to a straight line on our log-log scale.

APPENDIX C: EXPERIMENTS

The finite size effects captured by Eq. (B26) have also been observed in experiments. In these experiments, a rectangular block of silicon rubber (a nearly perfect elastic material even at large strain) is squeezed against hard, randomly rough surfaces. In this case, no plastic deformation will occur, and the compression of the rectangular rubber block, $(p/E')d$ (see below), which will contribute to the displacement s of the upper surface of the block, can be accurately taken into account. Such measurements were performed in Ref. [12] and were found to be in good agreement with the theory (these tests involved no fitting parameters, as the surface roughness power spectrum and the elastic properties of the rubber block were obtained in separate experiments). Here we show the result for the contact stiffness $K = -dp/d\bar{u}$ (not presented in Ref. [12]) of one additional such measurement.

The experiment was performed for a silicon rubber block (cylinder shape with diameter $D = 3$ cm and height $d = 1$ cm) squeezed against a road asphalt surface with the rms roughness amplitude 0.63 mm and the roll-off wavelength $\lambda_L \approx 0.3$ cm as inferred from the surface roughness power spectrum. The squeeze-force is applied via a flat steel plate and no slip of the rubber could be observed against the steel surface or the asphalt surface. We measured the displacement s of the upper surface of the block as a function of the applied normal load. Note that

$$s = (u_c - \bar{u}) + (p/E')d, \tag{C1}$$

where E' is the effective Young's modulus taking into account the no-slip boundary condition on the upper and lower surface, which was measured to be $E' = 4.2$ MPa in a separate experiment where the rubber block was squeezed between two flat steel surfaces. Using Eq. (C1) gives

$$K = -\frac{dp}{d\bar{u}} = -\frac{dp}{ds}\frac{ds}{d\bar{u}} = \frac{dp}{ds}\left(1 + \frac{Kd}{E'}\right) \tag{C2}$$

or

$$K = \frac{K^*}{1 - K^* d/E'}, \tag{C3}$$

where $K^* = dp/ds$. Using Eq. (C3), we obtain the results shown in Fig. 6, which presents the normal contact stiffness as a function of the applied nominal contact pressure obtained from the measured $p(s)$ relation with $E' = 4.2$ MPa (measured value) and $E' = 4$ MPa (to indicate the sensitivity of the result to E'). For very small contact pressures, $K^* \approx 0$ so that the denominator in Eq. (C3) is ≈ 1 (and $K \approx K^*$ as assumed in Ref. [20] without proof), and the result is insensitive to E', as also seen in Fig. 6. For large contact pressure, the experimental data exhibits rather large noise (and great sensitivity to E'), which originates from the increasing importance of the compression of the rubber block for large contact pressure.
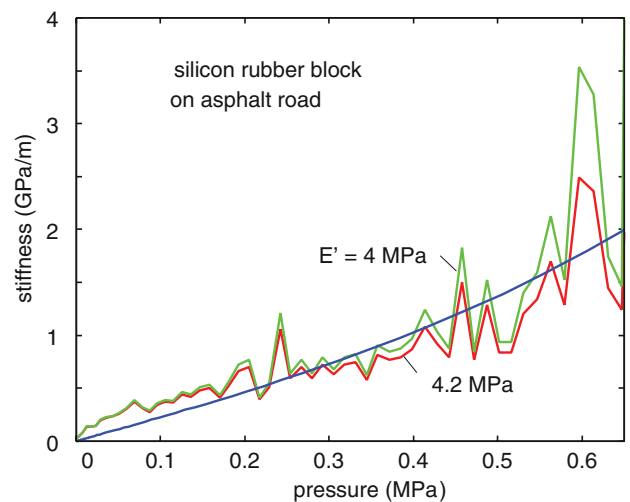

FIG. 6. (Color online) The normal contact stiffness as a function of the applied nominal contact pressure for a silicon rubber block (cylinder shape with diameter $D = 3$ cm and height $d = 1$ cm) squeezed against a road asphalt surface. The green and red lines are obtained from the measured $p(s)$ relation using Eq. (7) with $E' = 4.0$ and 4.2 MPa (see text), while the blue line is the theory prediction.

That is, for large pressures the denominator in Eq. (C3) almost vanishes, which implies that a small uncertainty in the measured $p(s)$ relation (which determines K^*), or in E', will result in a large uncertainty in K for large pressures.

The blue curve in Fig. 6 is the theory prediction, which is obtained without any fitting parameter using the measured surface roughness power spectrum. For small contact pressure, the contact stiffness obtained from the measured data is larger than predicted by the theory, but for nominal contact pressures typically involved in rubber applications (which are $\sim$0.4 MPa as in tire applications, or higher in most other applications), the finite-size effects are not important.

[1] F. P. Bowden and D. Tabor, *Friction and Lubrication* (Wiley, New York, 1956).

[2] J. H. Dieterich and B. D. Kilgore, Pure Appl. Geophys. **143**, 283 (1994).

[3] B. N. J. Persson, J. Chem. Phys. **115**, 3840 (2001).

[4] S. Hyun, L. Pei, J.-F. Molinari, and M. O. Robbins, Phys. Rev. E **70**, 026117 (2004).

[5] P. Berthoud and T. Baumberger, Proc. R. Soc. London A **454**, 1615 (1998).

[6] J. R. Barber, Proc. R. Soc. London A **459**, 53 (2003).

[7] J. A. Greenwood and J. B. P. Williamson, Proc. R. Soc. London A **295**, 300 (1966).

[8] B. N. J. Persson, Phys. Rev. Lett. **99**, 125502 (2007).

[9] G. Carbone and F. Bottiglione, J. Mech. Phys. Solids **56**, 2555 (2008).

[10] S. B. Ramisetti, C. Campañá, G. Anciaux, J.-F. Molinari, M. H. Müser, and M. O. Robbins, J. Phys.: Condens. Matter **23**, 215004 (2011).

[11] M. Benz, K. J. Rosenberg, E. J. Kramer, and J. N. Israelachvili, J. Phys. Chem. B **110**, 11884 (2006).

[12] B. Lorenz and B. N. J. Persson, J. Phys.: Condens. Matter **21**, 015003 (2009).

[13] L. Pei, S. Hyun, J. F. Molinari, and M. O. Robbins, J. Mech. Phys. Solids **53**, 2385 (2005).

[14] C. Yang and B. N. J. Persson, Phys. Rev. Lett. **100**, 024303 (2008).

[15] G. Carbone, M. Scaraggi, and U. Tartaglino, Eur. Phys. J. E **30**, 65 (2009).

[16] C. Campañá, B. N. J. Persson, and M. H. Müser, J. Phys.: Condens. Matter **23**, 085001 (2011).

[17] A. Almqvist, C. Campañá, N. Prodanov, and B. N. J. Persson, J. Mech. Phys. Solids **59**, 2355 (2011).

[18] S. Akarapu, T. Sharp, and M. O. Robbins, Phys. Rev. Lett. **106**, 204301 (2011).

[19] G. Carbone and F. Bottiglione, Meccanica **46**, 557 (2011).

[20] R. Pohrt and V. L. Popov, Phys. Rev. Lett. **108**, 104301 (2012).

[21] R. Pohrt, V. L. Popov, and A. E. Filippov, Phys. Rev. E **86**, 026710 (2012).

[22] C. Campañá and M. H. Müser, Europhys. Lett. **77**, 38005 (2007).

[23] C. Campañá, M. H. Müser, and M. O. Robbins, J. Phys.: Condens. Matter **20**, 354013 (2008); B. N. J. Persson, *ibid.* **20**, 315007 (2008).

[24] C. Campañá and M. H. Müser, Phys. Rev. B **74**, 075420 (2006).

[25] L. Pastewka, T. A. Sharp, and M. O. Robbins, Phys. Rev. B **86**, 075459 (2012).

[26] C. Campañá, Phys. Rev. E **78**, 026110 (2008).

[27] G. M. Pharr, W. C. Oliver, and F. R. Brotzen, J. Mater. Res. **7**, 613 (1992).

[28] J. R. Barber, Phys. Rev. E **87**, 013203 (2013).

[29] C. G. N. Pelletier, E. C. A. Dekkers, L. E. Govaert, J. M. J. den Toonder, and H. E. H. Meijer, Polym. Test. **26**, 949 (2007).

[30] W. B. Dapp, A. Lücke, B. N. J. Persson, and M. H. Müser, Phys. Rev. Lett. **108**, 244301 (2012).

[31] R. Buzio, C. Boragno, F. Biscarini, F. B. de Mongeot, and U. Valbusa, Nat. Mater. **2**, 233 (2003).

[32] B. Luan and M. O. Robbins, Nature (London) **435**, 929 (2005).

[33] C. L. Amba-Rao, J. Franklin. Inst. **287**, 241 (1969).

[34] K. L. Johnson, *Contact Mechanics* (Cambridge University Press, Cambridge, 1985).

[35] R. W. Hockney, in *Methods in Computational Physics,* Vol. 9, edited by B. Alder, S. Fernback, and M. Rotenberg (Academic Press, New York, 1970), pp. 135–211; see pp. 178-181.

[36] P. R. Nayak, J. Lubr. Technol. **93**, 398 (1971).